

THE AMiBA HEXAPOD TELESCOPE MOUNT

PATRICK M. KOCH¹, MICHAEL KESTEVEN², HIROAKI NISHIOKA¹, HOMIN JIANG¹, KAI-YANG LIN^{1,3}, KEIICHI UMETSU^{1,4},
YAU-DE HUANG¹, PHILIPPE RAFFIN¹, KE-JUNG CHEN¹, FABIOLA IBAÑEZ-ROMANO¹, GUILLAUME CHEREAU¹, CHIH-WEI
LOCUTUS HUANG^{3,4}, MING-TANG CHEN¹, PAUL T. P. HO^{1,5}, KONRAD PAUSCH⁶, KLAUS WILLMEROTH⁶, PABLO ALTAMIRANO¹,
CHIA-HAO CHANG¹, SHU-HAO CHANG¹, SU-WEI CHANG¹, CHIH-CHIANG HAN¹, DEREK KUBO¹, CHAO-TE LI¹, YU-WEI LIAO^{3,4},
GUO-CHIN LIU^{1,7}, PIERRE MARTIN-COCHER¹, PETER OSHIRO¹, FU-CHENG WANG^{3,4}, TA-SHUN WEI¹, JIUN-HUEI PROTY WU^{3,4},
MARK BIRKINSHAW⁸, TZIHONG CHIUH³, KATY LANCASTER⁸, KWOK YUNG LO⁹, ROBERT N. MARTIN¹⁰, SANDOR M. MOLNAR¹,
FERDINAND PATT¹¹, AND BOB ROMEO¹⁰

¹ Academia Sinica, Institute of Astronomy and Astrophysics, P.O. Box 23-141, Taipei 10617, Taiwan; pmkoch@asiaa.sinica.edu.tw

² Australia Telescope National Facility, P.O. Box 76, Epping NSW 1710, Australia

³ Department of Physics, Institute of Astrophysics & Center for Theoretical Sciences, National Taiwan University, Taipei 10617, Taiwan

⁴ Leung Center for Cosmology and Particle Astrophysics, National Taiwan University, Taipei 10617, Taiwan

⁵ Harvard-Smithsonian Center for Astrophysics, 60 Garden Street, Cambridge, MA 02138, USA

⁶ Vertex Antennentechnik GmbH, Duisburg, Germany

⁷ Department of Physics, Tamkang University, 251-37 Tamsui, Taipei County, Taiwan

⁸ Department of Physics, University of Bristol, Tyndall Avenue, Bristol BS8 1TL, UK

⁹ National Radio Astronomy Observatory, 520 Edgemont Road, Charlottesville, VA 22903, USA

¹⁰ Composite Mirror Applications, Inc., 1638 S. Research Loop 100, Tucson, AZ 85710, USA

¹¹ ESO Headquarters, Garching, Germany

Received 2008 November 11; accepted 2009 February 6; published 2009 March 25

ABSTRACT

The Array for Microwave Background Anisotropy (AMiBA) is the largest hexapod astronomical telescope in current operation. We present a description of this novel hexapod mount with its main mechanical components—the support cone, universal joints, jack screws, and platform—and outline the control system with the pointing model and the operating modes that are supported. The AMiBA hexapod mount performance is verified based on optical pointing tests and platform photogrammetry measurements. The photogrammetry results show that the deformations in the inner part of the platform are less than 120 μm rms. This is negligible for optical pointing corrections, radio alignment, and radio phase errors for the currently operational seven-element compact configuration. The optical pointing error in azimuth and elevation is successively reduced by a series of corrections to about 0.4 rms which meets our goal for the seven-element target specifications.

Key words: instrumentation; interferometers

1. INTRODUCTION

The Array for Microwave Background Anisotropy (AMiBA) is a dual-channel 86–102 GHz interferometer array of up to 19 elements with a resolution up to 2'. The AMiBA—located at the Mauna Loa weather station at an elevation of 3400 m on Big Island, Hawaii—targets specifically the distribution of high-redshift clusters of galaxies via the Sunyaev–Zel'dovich effect (e.g., Sunyaev & Zel'dovich 1972; Birkinshaw 1999 and references therein) and the anisotropies in the cosmic microwave background (CMB; e.g., Peacock 1999).

In the initial AMiBA operational phase, seven close-packed 0.6 m diameter Cassegrain antennas are co-mounted on a fully steerable platform controlled by a hexapod mount. The typical system noise temperature is ~ 100 K. From our observations we estimate a sensitivity of ~ 60 mJy in 1 hr. Previous progress reports were given in Li et al. (2006) and Raffin et al. (2006). The project as a whole, the correlator, and the receivers are described elsewhere (Ho et al. 2009; Chen et al. 2009). Observing strategy, calibration scheme, and data analysis with quality checks are described in Lin et al. (2009), Wu et al. (2009), and Nishioka et al. (2009). First AMiBA science results are presented in C.-W. Huang et al. (2009, in preparation), P. Koch et al. (2009, in preparation), G.-C. Liu et al. (2009, in preparation), Umetsu et al. (2009), and Wu et al. (2009).

In this paper, we describe the AMiBA mount, which is the largest operating astronomical hexapod mount. The role

of this paper is to provide additional instrumentation details about this novel hexapod, which complements the science papers. Section 2 introduces the hexapod mount, with more technical details about its components in Appendix A. Section 3 gives an overview of the pointing corrections and the control system. The explicit pointing model is presented in Appendix B. Photogrammetry measurements and detailed optical pointing tests verify the mount performance in Section 4. Our conclusions are given in Section 5.

2. HEXAPOD TELESCOPE

The design of the AMiBA mount was driven by the requirement of having a lightweight structure which can easily and quickly be dismantled and shipped to another site for a possible later relocation and the need of having direct access to the receivers on the platform for maintenance. The targeted science defined the operating frequency (86–102 GHz), and hence the required range of baselines, leading to a 6 m platform. Array configurations with maximum baselines require a pointing accuracy of ~ 0.2 . Based on these considerations, a hexapod mount with a carbon fiber reinforced plastic (CFRP) platform was chosen.

Whereas the concept of the hexapod (also called Stewart platform; Gough 1956; Stewart 1965) is successfully used in many technical applications such as machine tools, flight simulations, or complex orthopedic surgery, its application in

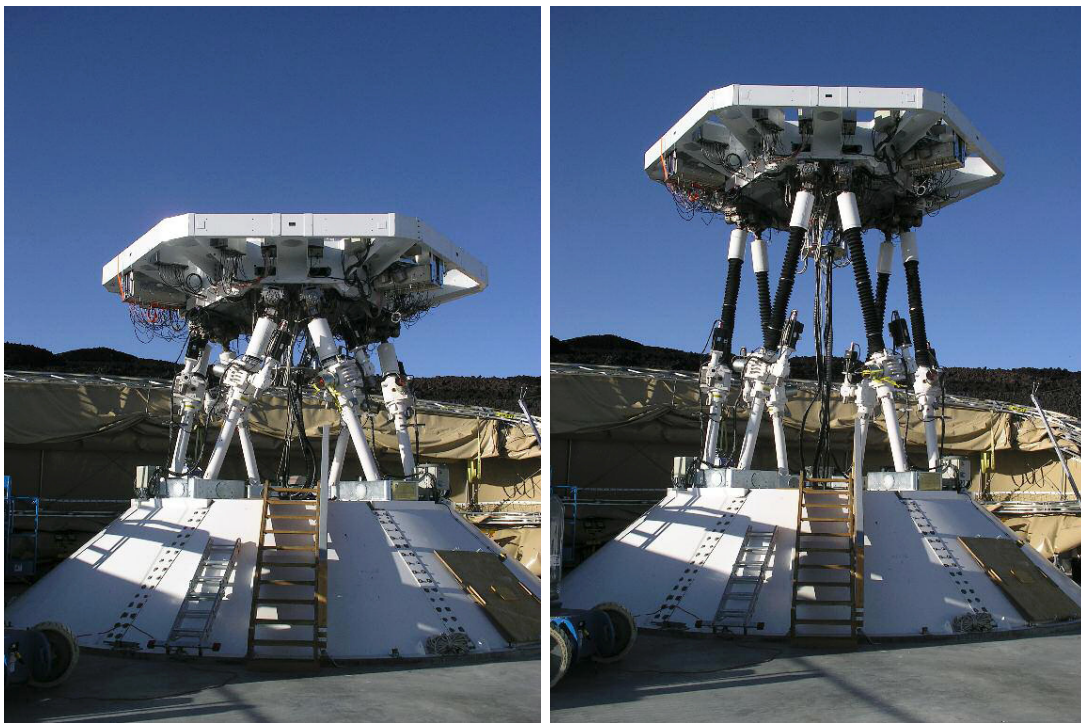


Figure 1. Left panel: the AMiBA in stow position with fully retracted jack screws of about 2.8 m length. In the back is the retractable shelter to protect the telescope. The height of the hexapod is about 5.5 m above ground level. Right panel: the AMiBA in neutral position with extended jacks to start the observation. The jack lengths are about 4.8 m and the telescope height is about 7.5 m above the ground.

astronomy has so far been mostly limited to secondary mirrors for classical Cassegrain telescopes, where the hexapod is used for focus optimization or wobbling movements to cancel the atmosphere and receiver noise. A pioneering design of a 1.5 m hexapod telescope for optical astronomy was presented in Chini (2000). Besides this, the AMiBA is the only operating hexapod telescope. The six independently actuated legs give the Stewart platform six degrees of freedom (x , y , z , pitch, roll, and yaw), where the lengths of the legs are changed to orient and position the platform. This parallel kinematics system has advantages and disadvantages compared to a serial kinematics system. There is no accumulation of position errors, and a generally lower inertia allows for faster accelerations and slewing velocities. The lower mass, however brings some risk for oscillations. The control system for the six legs is more complex, because of more degrees of freedom in motions which can compete and interfere with each other.

For astronomical applications the hexapod offers some interesting possibilities: no elevation counterweights and no azimuth bearing is needed and there is no zenith keyhole compared to a conventional mount. Access to the receivers and correlator from beneath the platform is straightforward. The sky field rotation (see Appendix C) can be compensated, and polarization measurements are possible by rotating the entire platform.

The AMiBA hexapod with its local control system was designed and fabricated by Vertex Antennentechnik GmbH, Duisburg, Germany. After a factory acceptance test in 2004 in Germany, the whole telescope was dismantled, shipped to Hilo, Hawaii, and assembled again on the Mauna Loa site with a final on-site acceptance test in 2005 October.

The key components in the Vertex design are: the upper and lower universal joints (u-joints) with jack screws, which require high stiffness and large travel ranges; the stiffness of the support cone, to minimize pointing errors from the cone; and the pointing error model required to meet the 0.2 pointing requirement.

The AMiBA hexapod has a lower limit of 30° in elevation. Azimuth movement is unlimited without interruption. The hexapod platform polarization (*hexpol*) range is limited to $\pm 30^\circ$, with the polarization rotation defined around the pointing axis at any possible mount position. Both limits are chosen for safety reasons based on structural concerns. Mechanical hard limit switches are in place to prevent movement beyond these limits in the case of software failure and overriding. The maximum slewing speed is 0.67 s^{-1} . The telescope is designed to meet the harsh environmental conditions on Mauna Loa, allowing us to operate with wind speeds of up to 30 m s^{-1} (for survival in stow position, wind speeds of up to 65 m s^{-1} can be tolerated) and an operating temperature range of -10°C to 30°C (in stow position: -30°C to 30°C). Earthquake survival conditions are met with 0.3 g for both horizontal and vertical accelerations. The total weight of the mount is $\sim 31,800\text{ kg}$. (Support cone $\sim 16,600\text{ kg}$, jack screws $\sim 6000\text{ kg}$, universal joints $\sim 9200\text{ kg}$.) The platform with the interface ring adds another $\sim 3000\text{ kg}$. The current load for the seven-element system is $\sim 500\text{ kg}$. The hexapod mount system, schematically illustrated in Figure 14, mainly consists of a support cone, six identical jack screw assemblies with gearboxes, drives and measuring systems, 12 u-joints in total, and a CFRP platform. More technical details about these components are given in Appendix A. Observations are started with extended jacks from a neutral position (Figure 1, right panel). The free access to receivers and correlator is shown in Figure 2.

3. CORRECTION SCHEME AND CONTROL SYSTEM: AN OVERVIEW

The hexapod topology is optimized with respect to minimized travel ranges of the u-joints and to minimized jack screw loads. Since the hexapod position is entirely determined by the variable length of the six jack screws together with the positions of

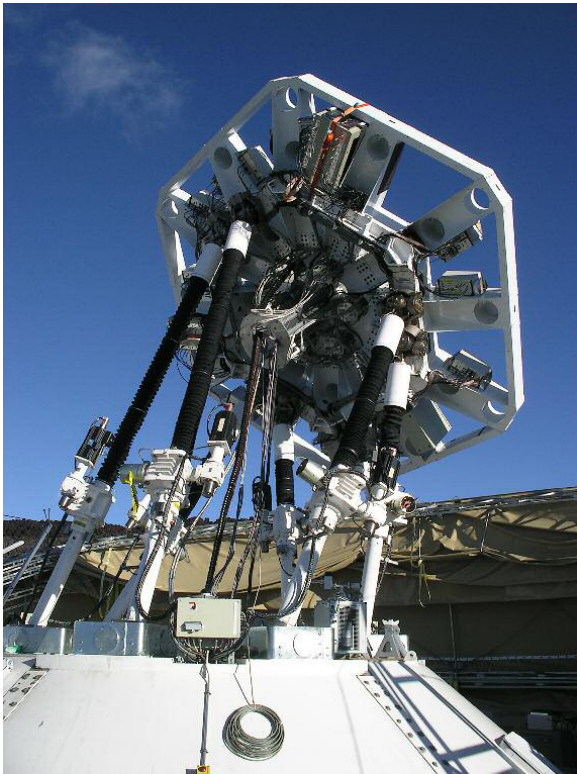


Figure 2. Rear view of the AMiBA showing the free access to all the receivers. Cables and helium lines are guided with a central fixed wrap in order to minimize the cable movement. A correlator box (topmost) and various receiver electronic boxes are mounted on the outer spokes of the platform.

the six lower fixed u-joints, utmost care needs to be taken to accurately monitor the jack screw lengths. The positions of the six lower fixed u-joints have been measured with a laser ranging system in the Vertex factory in Germany. The first group of pointing corrections on jack level consist of four compensations: jack screw pitch error, temperature compensation, jack screw rotation error, and support cone correction. They all directly yield a length correction for each individual jack at any given mount position. These error compensations have been tested and calibrated in the Vertex factory, and the correction algorithms are integrated into the hexapod control system. Besides the group of jack screw corrections, a second group of telescope pointing corrections is implemented: radio and optical refraction, an optical telescope (OT) collimation error correction, and an interpolation table (IT) for residual errors. Only the latter two ones need to be measured, updated, and handled by the operator. This second group leads to corrections in azimuth and elevation, which are then translated into jack corrections. A detailed description of the pointing error model is in Appendix B.

For radio observations, the OT collimation error correction is deactivated in the pointing error model. This assumes that the offsets derived from the optical pointing (with OT collimation correction, optical refraction, and all other corrections activated) are identical to the errors for the radio pointing (no collimation error correction, radio refraction, and all other corrections activated). In fact, the resolution and the collecting total power of the 0.6 m diameter antennas are not sufficient to do a separate radio pointing. However, we use the correlated signal to verify the relative radio alignment between individual antennas.

We remark that we do not derive explicit corrections for the platform polarization because the polarization stability and

precision have been found to be around 0.1 or better which is good enough for our purposes. We, however, derive azimuth and elevation pointing corrections for various platform polarizations (Section 4.2.2).

The main drive control and the jack length calculations for a commanded position are done by the antenna control unit (ACU). This also includes the inverse backward transformation giving the telescope position based on a set of jack lengths. This is essential for the continuous check between requested and actual telescope position, which is done in a closed loop system every 5 ms and updated depending on the operation. The above-mentioned pointing corrections are calculated on the pointing computer (PTC) where they can be individually activated and displayed. From here they are transferred to the ACU, illustrated in the flow chart in Figure 3.

The block diagram in Figure 4 summarizes the control system. The actual position, defined as the real position after applying all the pointing corrections, is displayed on ACU and reported to the remote telescope control system (TCS). A redundant-independent safety level is provided by the hexapod computer (HPC) with its programmable logic controller (PLC). The HPC calculates the telescope position from the jack positions as measured by the safety (auxiliary) encoders. The PLC is responsible for safety interlocks from limit switches. Time synchronization is derived from a stratum-1 GPS server, connected to the ACU with an IRIG-B time signal. Communication between individual computers is through standard LAN ethernet cables with TCP/IP protocol and NTP for time synchronization, and it is RS232 and/or CANbus where analog components are involved.

The telescope main operating modes include: *Preset*, *Star-track*, and *Protrack*, with the latter only possible in remote mode from TCS. *Preset* moves the telescope to a defined position in (Az , El , $hexpol$) on a geodesic path, ensuring a short and fast connection between subsequent mount positions. *Star-track* tracks a celestial object with either $hexpol = \text{const.}$ or $skypol = \text{const.}$ *Protrack* drives the telescope on a defined trajectory in (Az , El , $hexpol$, $time$) with a spline interpolation and a maximum stack of 2000 data points. This mode is extensively used for various types of observation and system checks.

4. PERFORMANCE VERIFICATION

In the initial AMiBA operational phase, seven close-packed 0.6 m diameter Cassegrain antennas (Koch et al. 2006) are used on baselines separated by 0.6 m, 1.04 m, and 1.2 m. The antenna field of view (FoV; FWHP $\sim 23'$) and the synthesized beam ($\sim 6'$) of the array in this configuration (at the observing frequency band of 86–102 GHz) set the specifications on the platform deformation and the pointing and tracking accuracy, which are: ~ 0.6 rms pointing error and a platform z direction deformation of less than 0.3 mm.

4.1. Platform Photogrammetry

Prior to the integration of the platform and the hexapod in Germany for the factory acceptance test, we performed stiffness measurements of the CFRP platform on the ground under expected loading conditions. These measurements were repeated at the Mauna Loa site. Both measurements showed that the deformations were larger than expected and predicted by finite element analysis (FEA), especially toward the outer edge of the platform, even after reinforcement was added. The cause is the segmented structure of the platform, coupled

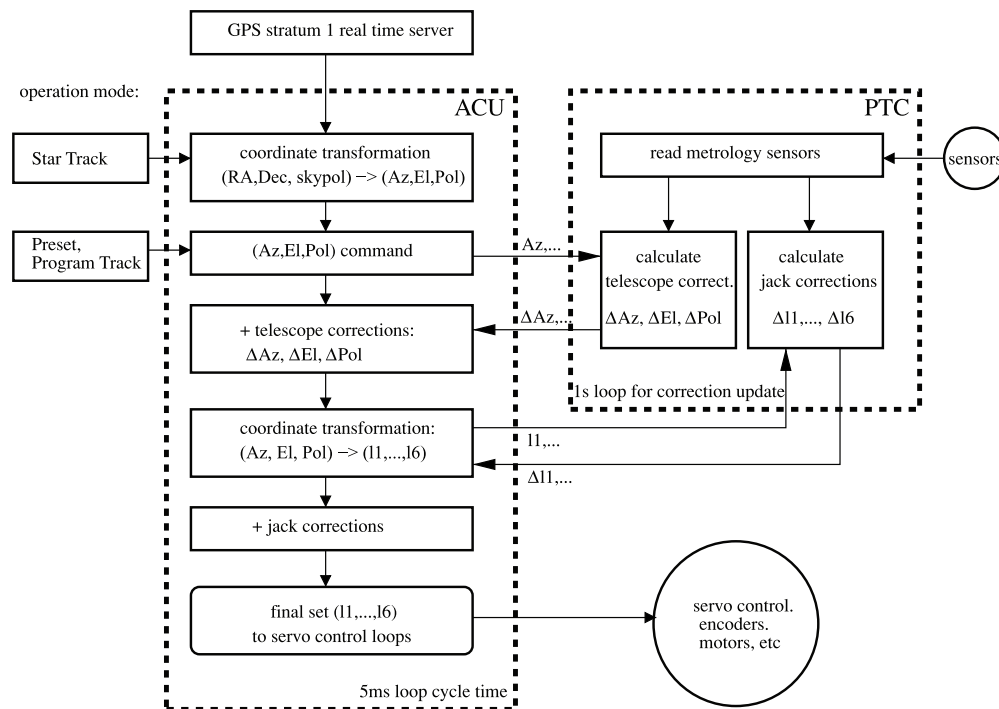


Figure 3. Flow chart illustrating the data transfer for the pointing corrections between the ACU and the PTC.

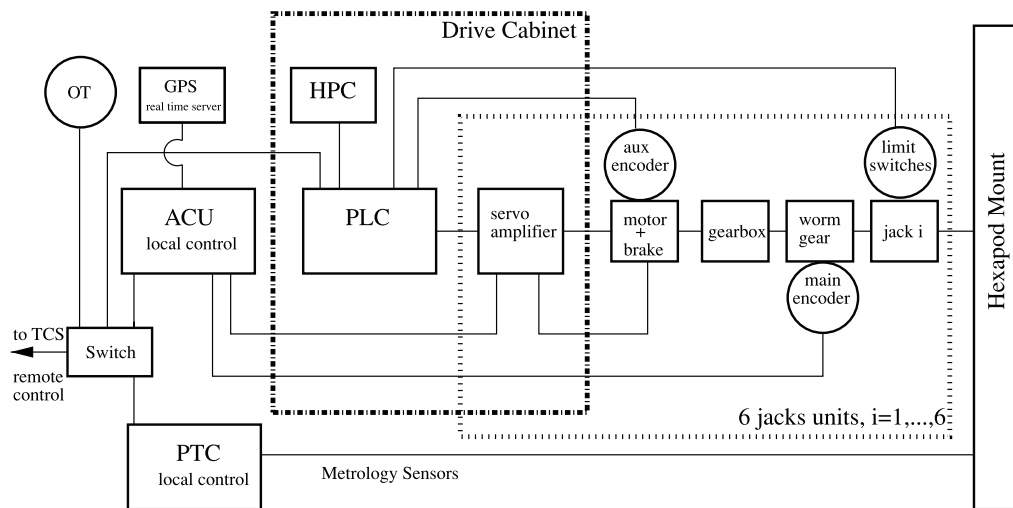


Figure 4. Block diagram of the local control system.

with inaccurate modeling of stiffness across the segment joints. It was decided to use the photogrammetry method to verify the platform deformations in a real seven-element compact configuration on the hexapod.

The first photogrammetry campaign took place during the fall of 2005, with dummy weights to replace receivers and electronic boxes. In 2006 October, we repeated the photogrammetry measurements, this time on the operational seven-element telescope. The results of the second survey are consistent with the 2005 results. In 2006, we achieved a better measuring accuracy: about $30 \mu\text{m}$ rms in z (defined as normal to the platform), with a short-term (1–2 days) and a long-term (1 week) repeatability better than $80 \mu\text{m}$ rms. We used a Geodetic Services, Inc. (GSI of Melbourne, Florida) INCA2 single digital photogrammetric camera. The pictures were processed with a GSI V-STARs three-dimensional industrial mea-

suring system. About 500 retro-reflective, self-adhesive targets (12 mm diameter, ~ 0.1 mm thick) were distributed over the entire platform surface with a higher target density around receivers. Fifty platform positions over the entire azimuth, elevation, and platform polarization range were surveyed.

The analysis of the photogrammetry measurements (Raffin et al. 2006; Huang et al. 2008) reveals a saddle-shaped platform deformation pattern at all surveyed positions, illustrated in Figure 5. The amplitude and phase of this saddle are functions of azimuth, elevation, and polarization. The specifications are met for the seven antennas in the compact configuration, with a z deformation amplitude up to 0.120 mm in the inner part of the platform. At the location of the OT, the maximum amplitude (measured at 30° elevation and 20° polarization) is about 0.38 mm (Figure 6), which leads to an OT tilt movement with respect to the normal pointing axis of the mount of

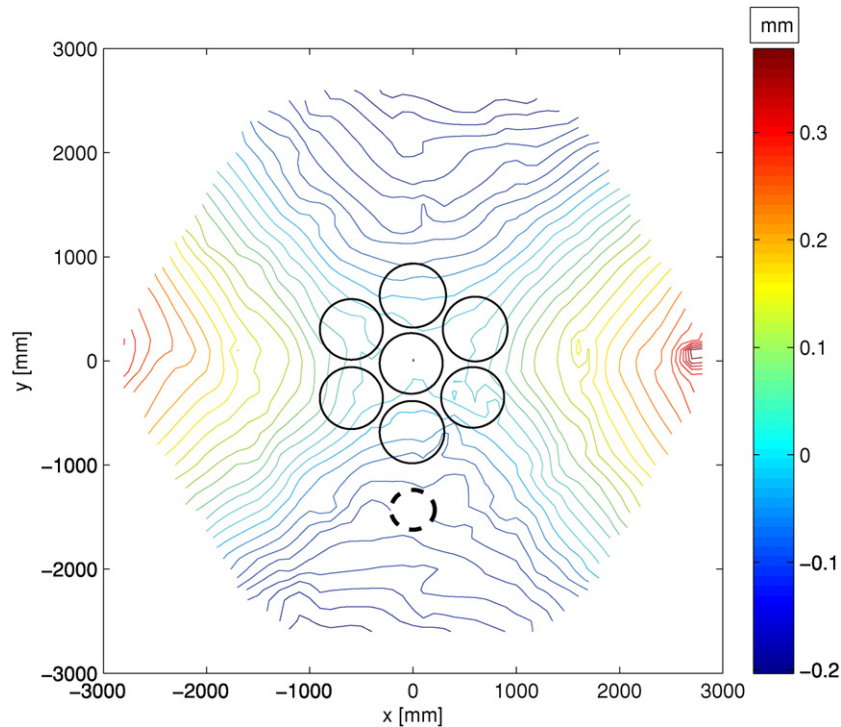


Figure 5. Contour plot of a typical platform saddle deformation in the z direction at the mount position $(Az, El, hexpol) = (0, 50, 0)$, in units of mm. The maximum deformations are about $+0.3$ mm and -0.2 mm at the outer edges of the platform. A roughly linear decrease in z deformations is seen toward the center of the platform. The locations of the OT (dashed circle) and the antennas (solid circles) are indicated for illustration.

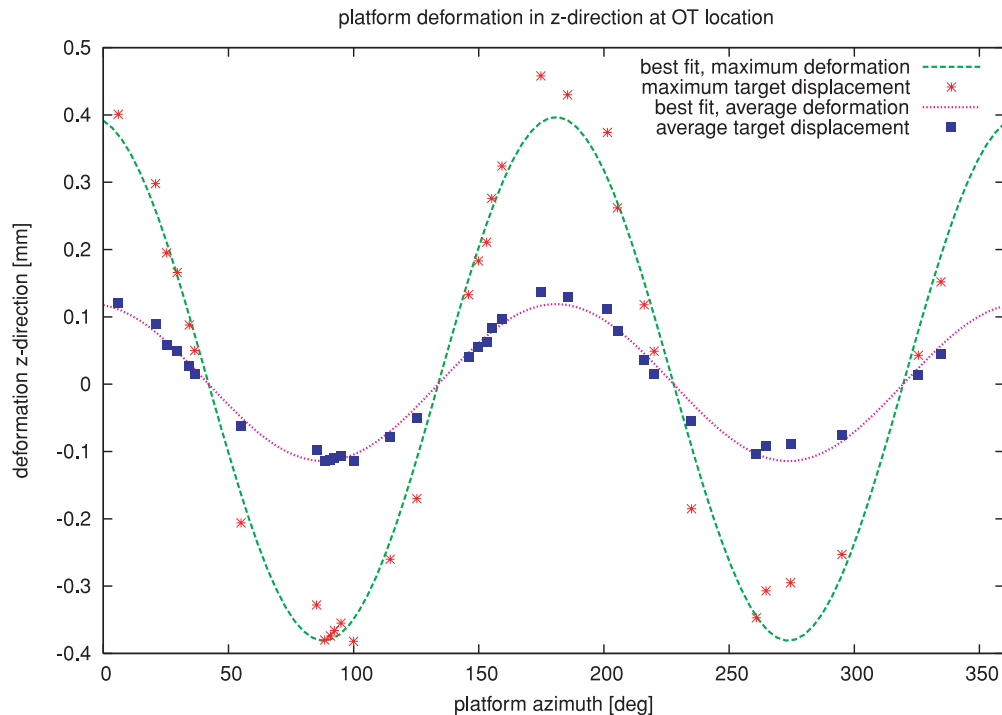


Figure 6. Platform deformation in the z direction as a function of platform azimuth at a radius $r = 1.4$ m where the OT is mounted. The selected data points are within an annulus of $r = 1.4 \pm 0.2$ m. The maximum deformation is measured at the extreme position $(Az, El, hexpol) = (0, 30, 20)$ and sets therefore an upper limit to this uncompensated pointing error. Also illustrated for comparison is an average mount position $(Az, El, hexpol) = (0, 60, 0)$ with an amplitude of about 0.11 mm, leading to a corresponding OT tilt of about $0'25$. Clearly visible is again the saddle structure with a functional form, $\cos(2Az)$.

about $\pm 1'$ in this extreme position. A more average position $(Az, El, hexpol) = (0, 60, 0)$ is also illustrated for comparison, showing an amplitude of about 0.11 mm, which leads to a corresponding OT tilt of about $0'25$. As argued in Section 4.2, this uncompensated pointing error is acceptable for the seven-

element compact configuration, but will need to be corrected for the planned expansion phase with 13 elements.

A detailed analysis and model of the saddle-type deformation for a 13-element radio phase correction and an error separation between deformation and pointing error is presented in Koch

et al. (2008). For this refined analysis we installed a second OT on the platform. By simply taking the difference between the two data sets of the two OTs, a characteristic signature appears which can be clearly attributed to the platform deformation. Using a saddle-type model as an input for the deformation, the mount pointing error can be successfully separated. Similarly, with the help of an interpolation scheme based on the entire photogrammetry data set, the radio phase error from the platform deformation can be reduced from a maximum of 800 μm rms over the entire platform to 100 μm or less. The synthesized beam area is then maintained to within 10% of its nondeforming ideal value. In this way, the specifications are also met for the 13-element expansion.

4.2. Hexapod Optical Pointing

Pointing with a hexapod telescope is different from a conventional telescope where a 7- or 13-parameter pointing error model is often used. An important consequence of the hexapod mount is the absence of azimuth and elevation encoders as compared to more traditional telescopes. The three-dimensional locations of the upper and lower u-joints in the measured reference positions and the jack lengths in any position completely define the geometry of the mount. The pointing error model therefore needs to take utmost care in treating the jack lengths and the lower u-joint positions. The six upper u-joint locations define a best-fit plane with its normal defining the resulting pointing axis.

Optical pointing is carried out with a Celestron C8 telescope, equipped with a Fastar $f/1.95$ adapter lens and an SBIG ST-237 CCD camera. The resulting FoV is about $30' \times 20'$ on a 652×495 pixel array, giving a calibrated pixel scale of about $3''/81$. A preliminary rough OT collimation error is measured on the platform with a digital tiltmeter and compensated in the pointing error model, following Equations (B8) and (B9).

4.2.1. Pointing with $hexpol = 0$

In order to achieve the required pointing accuracy of $0.6''$ or better, a two-step approach is adopted. In a first pointing run, all the known pointing corrections (Section 3) except the IT are activated on the PTC. As a function of the mount position, $(Az, El, hexpol = 0)$, the offsets $(\Delta x_k, \Delta y_k)$ of a target star k , with respect to the center of the CCD image, are split into an Az and El error in a common reference frame at $Az = 0$. This involves rotating the CCD images by the mount Az (and $hexpol$) coordinate, together with an additional rotation γ for the orientation of the CCD with respect to the sky. This yields the CCD frame–mount frame transformation (Figure 7):

$$\begin{pmatrix} \Delta Az_{\text{raw},k} \\ \Delta El_{\text{raw},k} \end{pmatrix} = \begin{pmatrix} \cos \beta_k & \sin \beta_k \\ -\sin \beta_k & \cos \beta_k \end{pmatrix} \begin{pmatrix} \Delta x_k \\ \Delta y_k \end{pmatrix}, \quad (1)$$

where $\beta_k = Az_k + hexpol_k + \gamma$ for each star image k at the mount position k . The raw errors $(\Delta Az_{\text{raw},k}, \Delta El_{\text{raw},k})$ are then analyzed to separate the remaining uncompensated OT collimation error from the real mount pointing error. $(\Delta Az_{\text{coll,OT}}, \Delta El_{\text{coll,OT}})$ has a characteristic azimuth and elevation signature of the form

$$\begin{pmatrix} \Delta Az_{\text{coll,OT}} \\ \Delta El_{\text{coll,OT}} \end{pmatrix} = \begin{pmatrix} C_{Az} \\ C_{El} \end{pmatrix} + A \begin{pmatrix} \cos(Az + \phi) \\ \cos(Az + \phi + \pi/2) \end{pmatrix}, \quad (2)$$

where A and ϕ are the OT uncompensated tilt amplitude and phase, respectively, which reflect the remaining OT collimation

error and (C_{Az}, C_{El}) are two constants. Assuming a rigid OT, the amplitude A is identical for the azimuth and elevation signature and their phases are separated by $\pi/2$. The small fitting residuals $\Delta \bar{Az}_{\text{IT}}, \Delta \bar{El}_{\text{IT}}$ (of the order of $1''$ or less) populate the IT, which is a three-dimensional table in Az , El , and $hexpol$:

$$\begin{pmatrix} \Delta \bar{Az}_{\text{IT},k} \\ \Delta \bar{El}_{\text{IT},k} \end{pmatrix} = \begin{pmatrix} \Delta Az_{\text{raw},k} \\ \Delta El_{\text{raw},k} \end{pmatrix} - \begin{pmatrix} \Delta Az_{\text{coll,OT}} \\ \Delta El_{\text{coll,OT}} \end{pmatrix} + \begin{pmatrix} C_{Az} \\ C_{El} \end{pmatrix}. \quad (3)$$

The irregular grid errors $(\Delta \bar{Az}_{\text{IT},k}, \Delta \bar{El}_{\text{IT},k})$ are then transformed into a regular spaced grid with the cubic Shepard algorithm (Renka 1999), finally generating the IT pointing corrections $(\Delta Az_{\text{IT}}, \Delta El_{\text{IT}})$.

In a second pointing run, all the known pointing corrections and the IT are activated on the PTC. This verifies that the mount errors are reduced with the IT and that only the OT collimation error remains. These small errors are checked every few weeks for their repeatability. Typically, one IT iteration is needed to reduce an initial pointing error in Az and El from $\sim 1''$ rms to about $\sim 0.4''$ rms. Subsequent pointing tests have revealed almost exactly the same numbers (within repeatability, Section 4.3), so that our IT has been unchanged over the year of data-taking. The iterative improvement with the IT is illustrated

in Figure 8, where the total raw error, $\sqrt{\Delta Az_{\text{raw},k}^2 + \Delta El_{\text{raw},k}^2}$, is shown in a polar plot over the entire azimuth range. In this strategy, it is crucial to identify properly the remaining uncompensated OT collimation error $(\Delta Az_{\text{coll,OT}}, \Delta El_{\text{coll,OT}})$ to make sure that the small remaining values in the IT compensate only and exclusively for the hexapod mount errors. For radio observations, the OT collimation error correction is deactivated in the pointing error model. This assumes that the pointing errors derived from the optical pointing (with OT collimation correction, optical refraction and all other corrections activated) are identical to the errors for the radio pointing (no collimation error correction, radio refraction, and all other corrections activated). No separate radio pointing is done because the 0.6 m antennas (FWHM $\sim 23'$) do not have enough gain to allow us to verify the required pointing accuracy. In order to have the most rigid measure, the OT is installed close to one of the upper u-joint positions. Possible local irregularities and position-dependent platform deformations, which can affect the rigidity of the OT, need to be filtered out if the pointing needs to be further improved (Koch et al. 2008).

The IT approach further assumes that the remaining mount errors are sufficiently smooth enough functions in between neighboring pointings, leading to the question of the optimized pointing cell size. We find that 100 stars, approximately evenly distributed in solid angle over the entire accessible sky, resolve the pointing features reasonably well. Observing more stars does not significantly improve the pointing. Typically, we need about 1 hr to observe 100 stars in a fully automatic mode, where the telescope is driven from high to low elevation on a spiraling trajectory.¹² A multiple of this time is required if different platform polarizations for each star are included.

Although not necessary in the IT approach, we found it useful to further analyze the residuals and identify their origins. A more

¹² In the initial phase, the mount and pointing performance were extensively tested by driving the telescope manually from a few randomly chosen initial positions to the same target position. These tests indeed helped to identify flaws in the control software. Subsequently, with the stable control algorithm, different trajectories were found to be equivalent. For the automatic mode, a spiraling trajectory was then adopted because this leads to the most efficient sky coverage with a minimized overhead in telescope drive time.

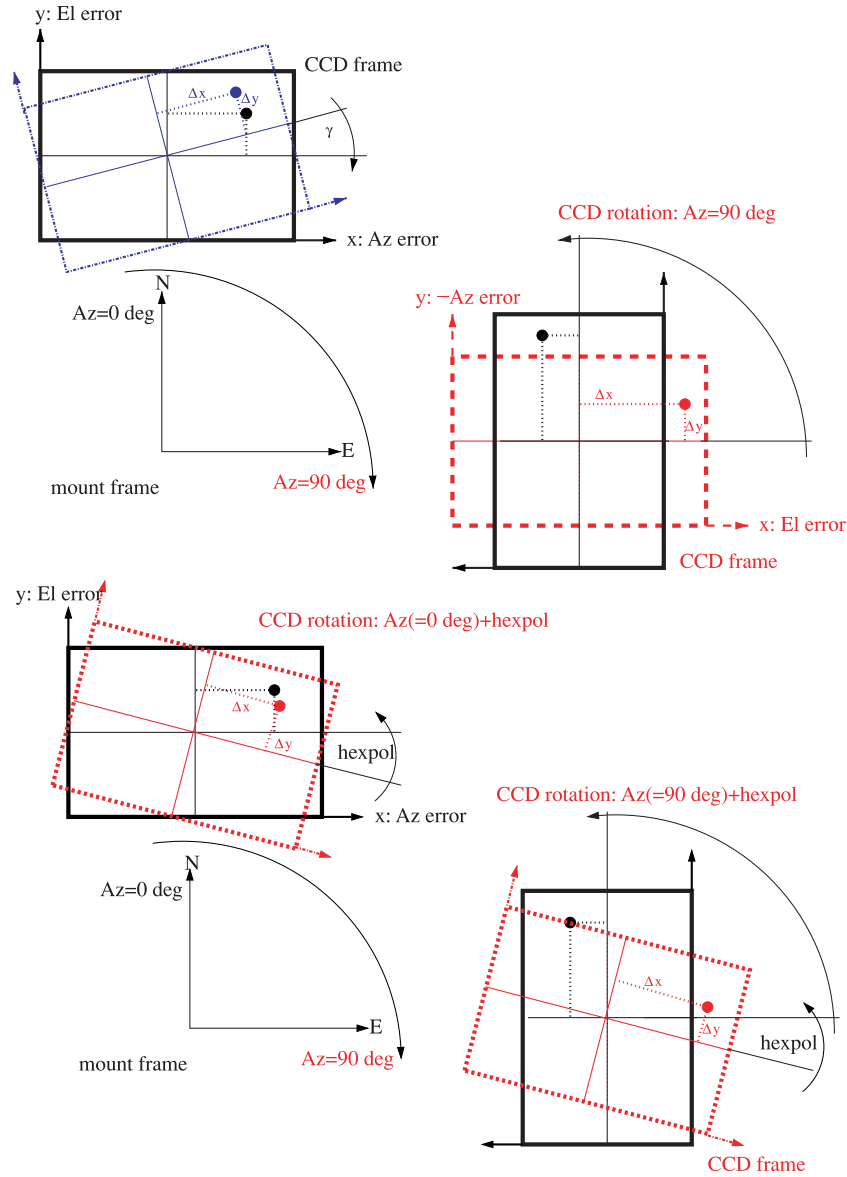


Figure 7. Illustration of the CCD frame–mount frame transformation. Measured star position offsets are indicated with Δx and Δy . Top panel: the rotation γ aligns the CCD frame with the east–west sky drift direction (blue–black frames). At the reference position $Az = 0^\circ$, the CCD axes then directly measure azimuth and elevation errors. Moving to different azimuth positions only tips (but not rotates) the CCD frame, illustrated at $Az = 90^\circ$ with the red-dashed CCD frame. A rotation of 90° brings it back to the reference position. The original blue frame before sky drift alignment is omitted here. Bottom panel: additional platform polarization (*hexpol*) which rotates the CCD frame (red dashed). A rotation of $Az + \text{hexpol}$ brings them back to the reference position. The blue frame is again omitted here for clarity.

detailed fitting including the mount tilt:

$$\begin{pmatrix} \Delta A_{z, \text{raw}, k} \\ \Delta E_{l, \text{raw}, k} \end{pmatrix} = \begin{pmatrix} \Delta A_{z, \text{coll}, \text{OT}} \\ \Delta E_{l, \text{coll}, \text{OT}} \end{pmatrix} + B \begin{pmatrix} \cos(Az + \psi) \times \sin(El) \\ \cos(Az + \psi + \pi/2) \end{pmatrix},$$

where $(\cos(Az + \psi) \times \sin(El), \cos(Az + \psi + \pi/2))$ is a term taking into account an additional mount tilt, improved the goodness of the fit only marginally, but still revealed a mount cone/foundation tilt of $\sim 0'.2$ with respect to the zenith. Furthermore, our control software allows us to simulate a small rotation of the entire telescope. In this way, we identified a slight misorientation of the cone with respect to the north of $\sim 1'$. These effects contribute partly to the constants (C_{Az}, C_{El}) in Equation (2). Since both errors are small, we simply absorb them in the IT.

4.2.2. Pointing with *hexpol* $\neq 0$

Extracting the polarization corrections relies on the proper identification of the OT signature. This is best done at *hexpol* =

0, since at *hexpol* $\neq 0$ the polarization error and the OT signature become degenerate. The *hexpol* movement is illustrated in Figure 9. For the OT itself, the *hexpol* $\neq 0$ case is only an additional rotation, identical to an azimuth position with $az + \text{hexpol}$, as described in Equation (1). We are thus extracting the OT signature at *hexpol* = 0 assuming it to be rigid enough, so that any position error with a polarized platform, as a function of (Az, El, hexpol) , becomes

$$\begin{pmatrix} \Delta \tilde{A}_{z, \text{IT}, k} \\ \Delta \tilde{E}_{l, \text{IT}, k} \end{pmatrix} = \begin{pmatrix} \Delta A_{z, \text{raw}, k} \\ \Delta E_{l, \text{raw}, k} \end{pmatrix} - \begin{pmatrix} \Delta A_{z, \text{coll}, \text{OT}} \\ \Delta E_{l, \text{coll}, \text{OT}} \end{pmatrix}_{\text{hexpol}_k} + \begin{pmatrix} C_{Az} \\ C_{El} \end{pmatrix},$$

where $(\Delta A_{z, \text{raw}, k}, \Delta E_{l, \text{raw}, k})$ are again defined as in Equation (1) with *hexpol* $\neq 0$ and $(\Delta A_{z, \text{coll}, \text{OT}}, \Delta E_{l, \text{coll}, \text{OT}})_{\text{hexpol}_k}$ are the OT signatures shifted by *hexpol*_k, $Az_k \rightarrow Az_k + \text{hexpol}_k$ in Equation (2). This is illustrated in Figure 10 for the raw elevation errors, where polarization pointing was done

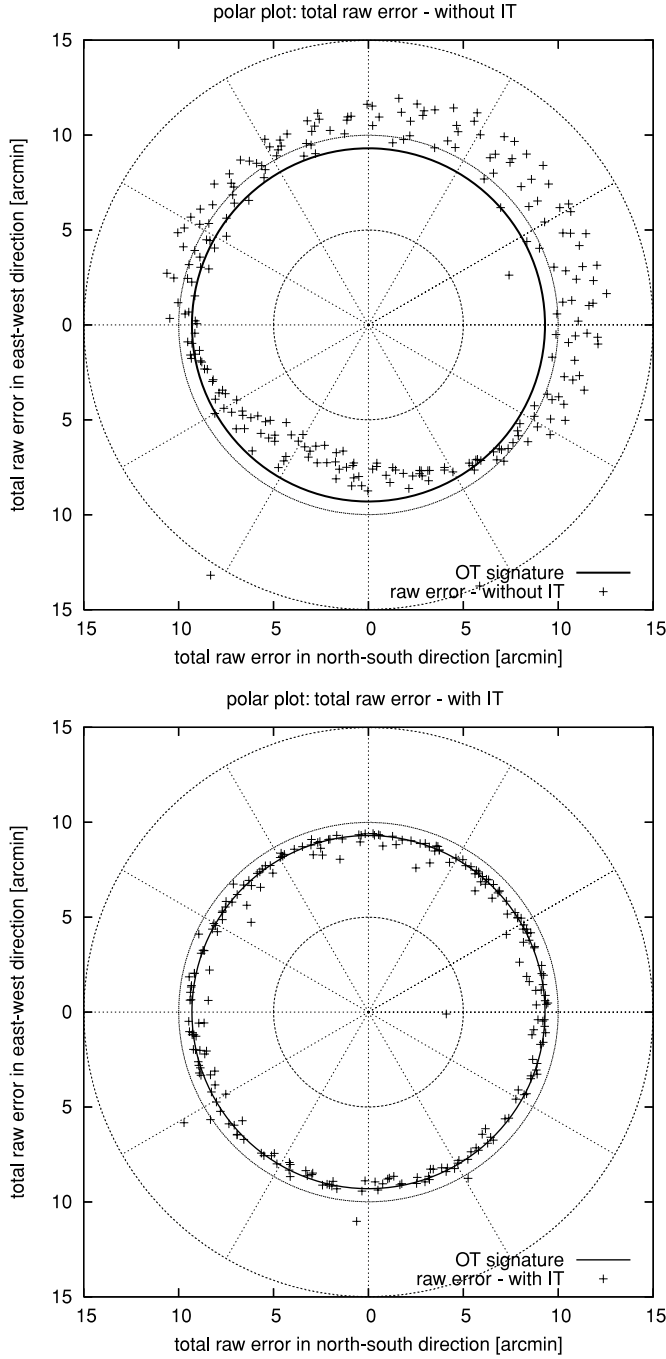


Figure 8. Top panel: polar plot of the total raw error, combining $\Delta A_{z,raw,k}$ and $\Delta E_{l,raw,k}$, without IT correction. The remaining uncompensated OT collimation error (OT signature) is shown as a circle which represents the OT tilt $\sim 9'$ with respect to the mount pointing axis. The data points scattered off the circle show the residual pointing errors $\Delta A_{z,IT,k}$ and $\Delta E_{l,IT,k}$ for the IT, leading to $\sim 1'$ rms pointing error. The test was done with 250 stars. Bottom panel: polar plot of the total raw error with IT correction. The OT collimation error is again shown as a circle. The reduced scatter compared to the top panel verifies the improved pointing with ~ 0.4 rms pointing error.

with $hexpol = \pm 20^\circ, \pm 10^\circ$, and 0° for 100 stars. Clearly seen is the OT signature with the $hexpol = 0$ case shifted to the different $hexpol$ angles. The residual polarization errors increase linearly with the polarization angle, from ~ 0.8 to $\sim 3'$ for 0° to 20° , as shown in Figure 11 for the polarization-dependent elevation error. We remark that we do not explicitly correct for a polarization error. We found that

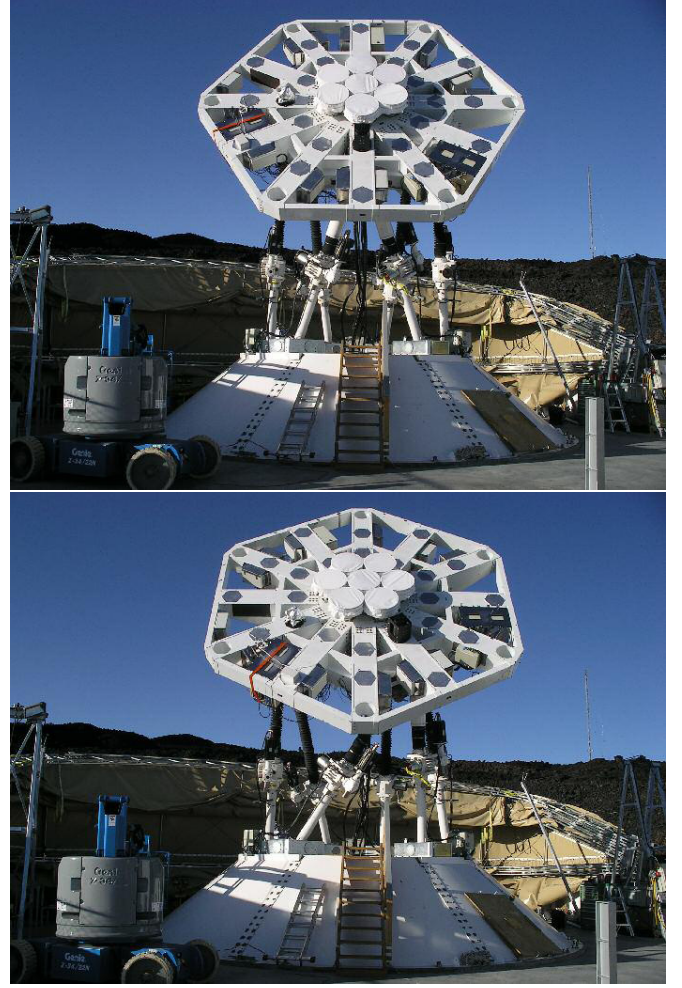


Figure 9. Top panel: front view of the AMiBA with a platform polarization $hexpol = 0$. Installed are seven antennas in compact configuration, giving 0.6 m, 1.04 m, and 1.2 m baselines. Free receiver holes in the CFRP platform allow for different array configurations and for a planned expansion phase with 13 antennas. The 8 inch refractor for optical pointing is attached to the black bracket below the lowermost antenna at a distance of 1.4 m from the platform center. Bottom panel: front view of the AMiBA with a platform polarization $hexpol = 30$. (Counterclockwise rotation with respect to the top panel.)

the uncertainty in the polarization angle is within 0.1 or better, which is negligible for the later pointing error analysis and our observations.

We finally consider the influence of the platform deformation (Section 4.1) on the pointing error analysis. The local saddle-type deformation with a z direction amplitude of typically $100 \mu\text{m}$ at the OT radius will slightly change the OT's phase and amplitude as a function of the mount position, and therefore introduce a local position-dependent error which is under/overcompensated in the IT. However, a $100 \mu\text{m}$ amplitude leads to an estimated wiggling of the OT of about $0.25'$. For the seven-element compact configuration, we consider that acceptable and we therefore have not further extracted this component.

4.3. Repeatability

A key parameter to ensure the reliability of the entire system is the pointing repeatability. Factory tests have revealed short-term repeatability errors between $1''$ and $7''$ in Az and El ,¹³ respectively. Two astronomical tests with the OT were

¹³ For these tests, a laser source was installed on the platform. The mount was repeatedly driven to the same target position after going back to an initial

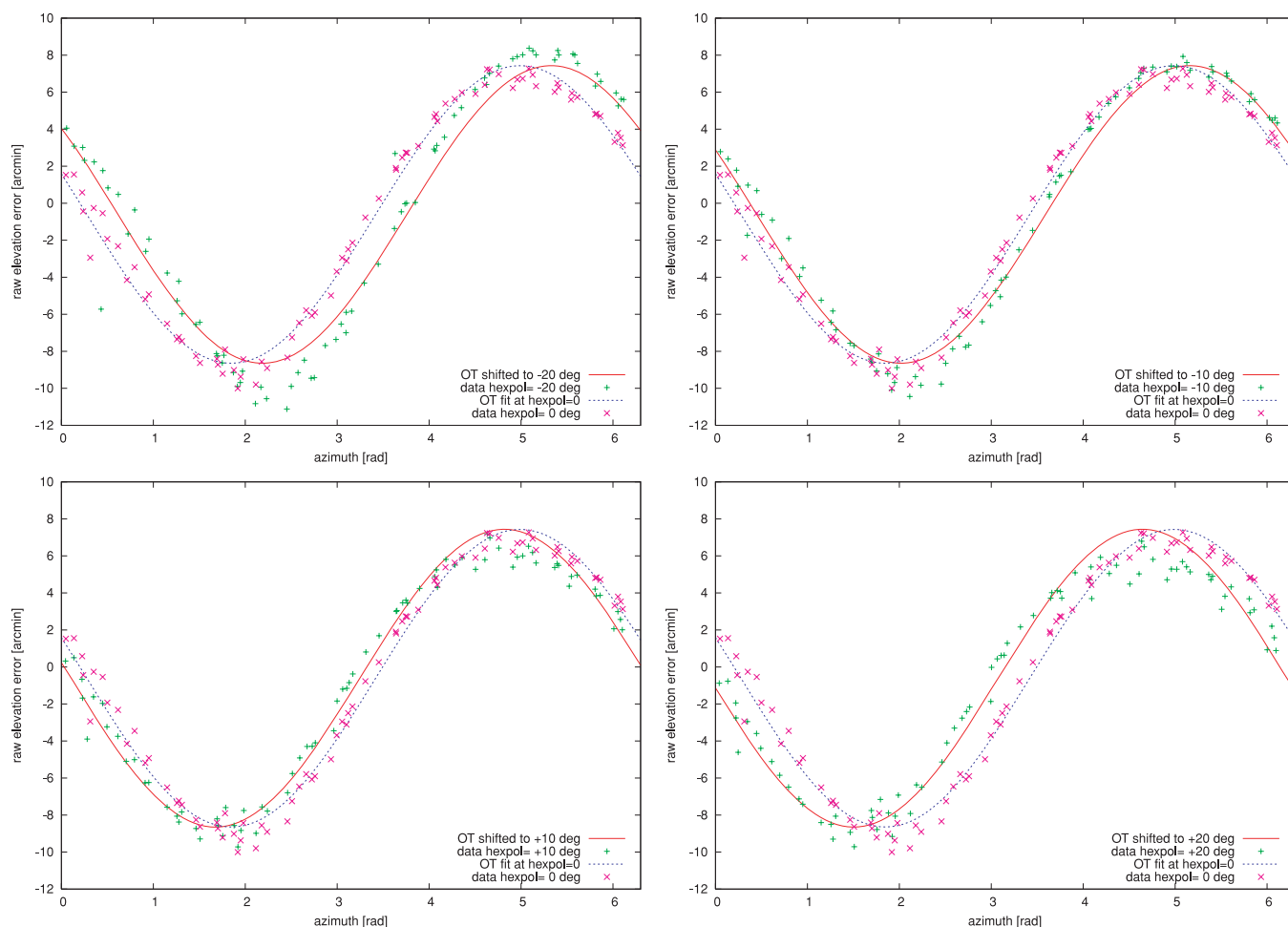


Figure 10. Raw elevation errors (including remaining OT collimation error apparent as a cosinelike signature) for $hexpol = -20^\circ, -10^\circ, +10^\circ$, and $+20^\circ$, displayed in the panels from left to right and top to bottom. An OT signature extracted from the $hexpol = 0$ pointing data is shifted to the $hexpol \neq 0$ data to calculate the residual errors for the IT.

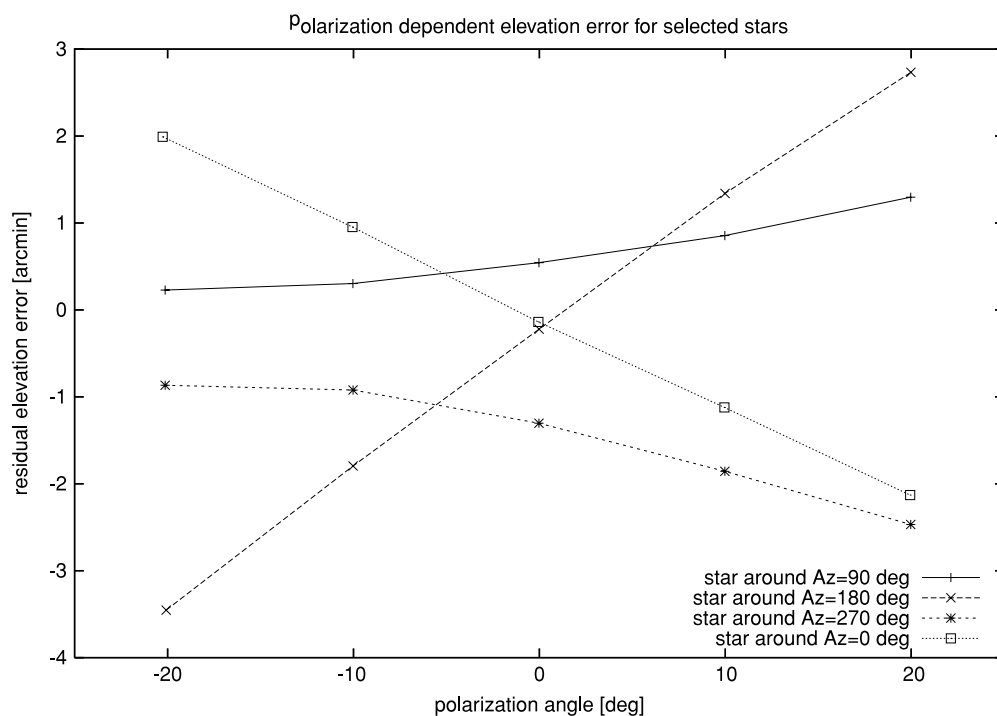


Figure 11. Elevation error residuals after extracting the OT signature for selected stars at $Az = 0^\circ, 90^\circ, 180^\circ$, and 270° as a function of $hexpol$. Errors tend to increase linearly toward larger polarization angles. The azimuth errors (not shown) manifest the same result.

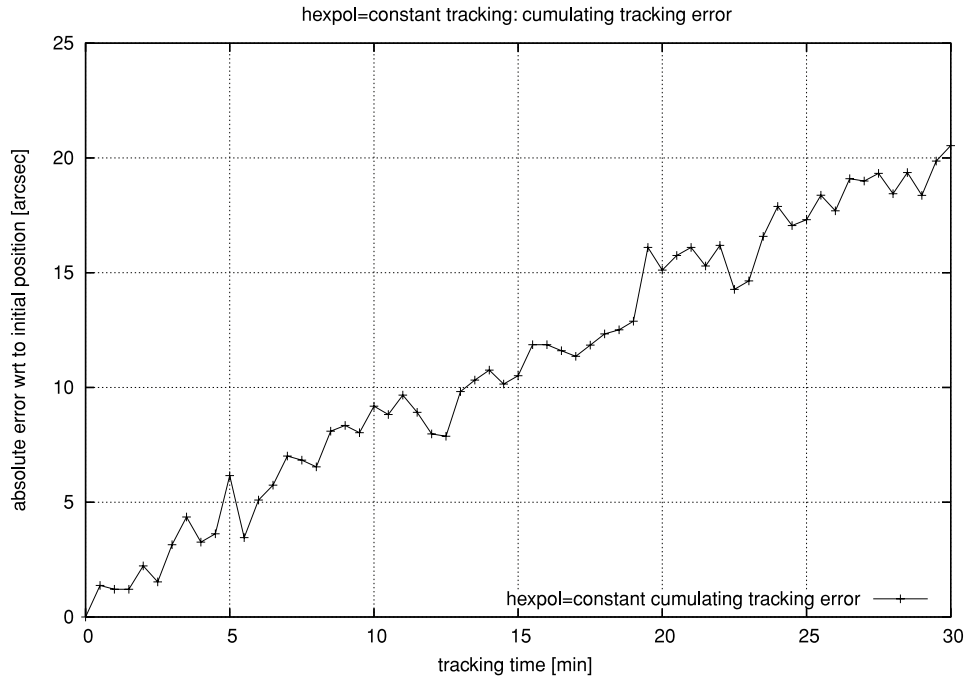


Figure 12. Tracking accuracy in *hexpol* = const. mode, accumulating linearly to a tracking error of about 20'' after 30 minutes.

performed: first, in an overall repeatability test, two runs with 250 stars (distributed on equal solid angles over the complete accessible celestial sphere) were executed during the same night, the second run immediately after the first one, with almost identical atmospheric conditions. Second, in a star position test, aiming at the day-to-day repeatability, a set of eight stars in different directions and elevations was observed on two subsequent days at the same time. CCD images were then taken by going back and forth between two stars of this set. Some stars could be observed at almost exactly the same time at almost identical mount positions. Both tests show consistent results: a cell-to-cell comparison from the overall repeatability test gives an average *Az* and *El* error difference of 5''.7 and 2''.5, respectively. The star position tests show a day-to-day repeatability better than 4''. From the same test, it could also be verified that small changes in the mount position introduce only small linear deviations in the pointing and tracking errors.

The long-term repeatability has been checked on a roughly weekly basis in the early mount testing phase. Later, with each additional receiver element integrated into the array, pointing tests have been routinely carried out. All these results are consistent within the short-term repeatability errors. Over more than two years operation of the seven-element compact configuration, a very robust pointing performance was verified, with no measurable changes due to temperature or other environmental effects, or additional weight on the platform.

4.4. Tracking

Tracking tests were performed over short time periods, typically about 30 minutes. This ensures that tracking results are not or only minimally biased by any uncompensated pointing errors. 30 minute tests mean that pointing stars remain within a single IT cell. The tracking tests were done in both polarization

modes, *hexpol* = const. and *skypol* = const.¹⁴ In the *hexpol* = const. mode, a linearly increasing tracking error was measured over 30 minutes, accumulating to 20'' after 30 minutes in Figure 12. The *skypol* = const. mode shows a field rotation stability of about 3/6 rms with respect to an initial polarization direction over 30 minutes, Figure 13. Since tracking is internally handled as a fast sequence of pointing positions, the long-term tracking error (several hours or large ranges in *Az*, *El*, and *hexpol*) is controlled by all the pointing corrections including the IT. On short timescales (within interpolated errors in the IT), the measured tracking error reflects a combination of partially uncompensated pointing errors and tracking-specific errors.¹⁵ Our normal observations (Wu et al. 2009) are carried out in a lead/trail-main field procedure over about 6 minutes. The tracking error is therefore negligible.

4.5. Array Efficiency

Based on the measured pointing accuracy, we quantify the array efficiency. Besides this absolute mount pointing error (*p*), which misaligns each antenna by the same amount, we also take into account the measured platform deformation error (*d*) and a radio misalignment error (*m*) for each antenna pair (baseline). *d* and *m* define a relative error which measures the shift in the overlap of two antenna primary beams. Additionally,

¹⁴ *hexpol* = const.: a celestial object is tracked by keeping the intrinsic platform polarization constant. In this mode, any possible complication from the additional polarization movement is avoided, making it a clean measure of tracking performance. In order to separate the tracking and pointing errors, tracking is done only over a short time (small angular range), where the pointing error is supposed not to change significantly. Longer tracking tests require the use of the IT. *skypol* = const.: a celestial object is tracked by fixing a polarization on the sky, introducing therefore a counter-rotation of the hexapod to compensate for the sky rotation. This checks the tracking stability of the mount. Constant *skypol* mode is essential for polarization measurement and control of baseline orientations. We test this mode by monitoring the orientation of a vector between two stars.

¹⁵ Tracking-specific errors result from the moving telescope, contrary to the pointing errors where the telescope accuracy is measured at a fixed position. However, on a short timescale, tracking errors are typically small, and they are therefore not further taken into account in the analysis.

position. The slight shifts in the locations of the projected laser beams on the factory wall were then used to characterize the repeatability at the target positions.

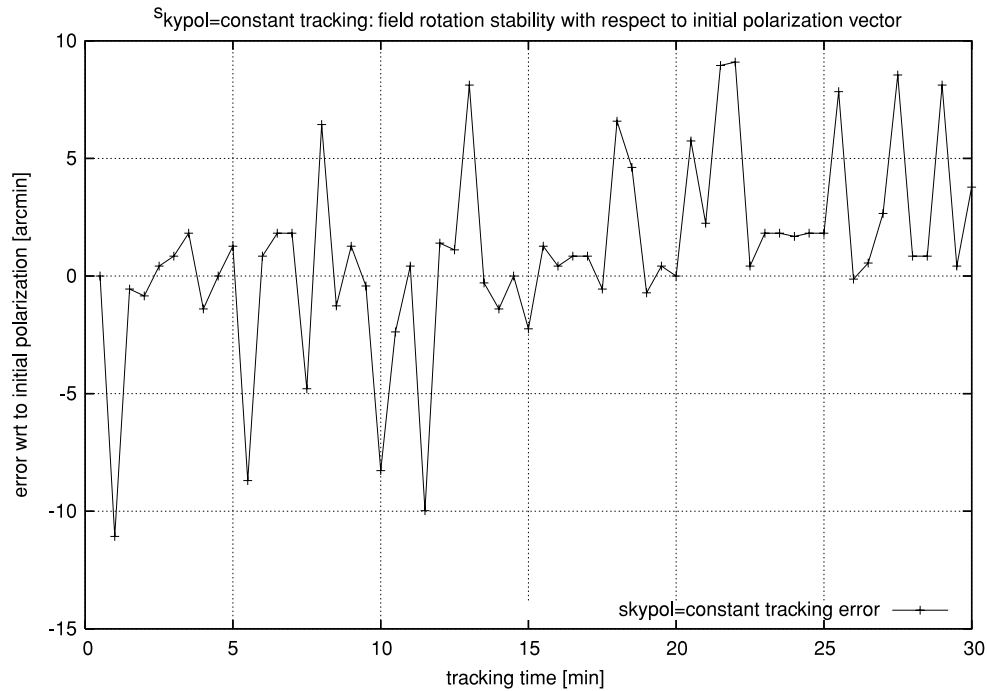


Figure 13. Field rotation stability test in $skypol = \text{const.}$ mode, showing about $4'$ rms accuracy in the control of the rotation angle. Subsequent images are separated by 30 s.

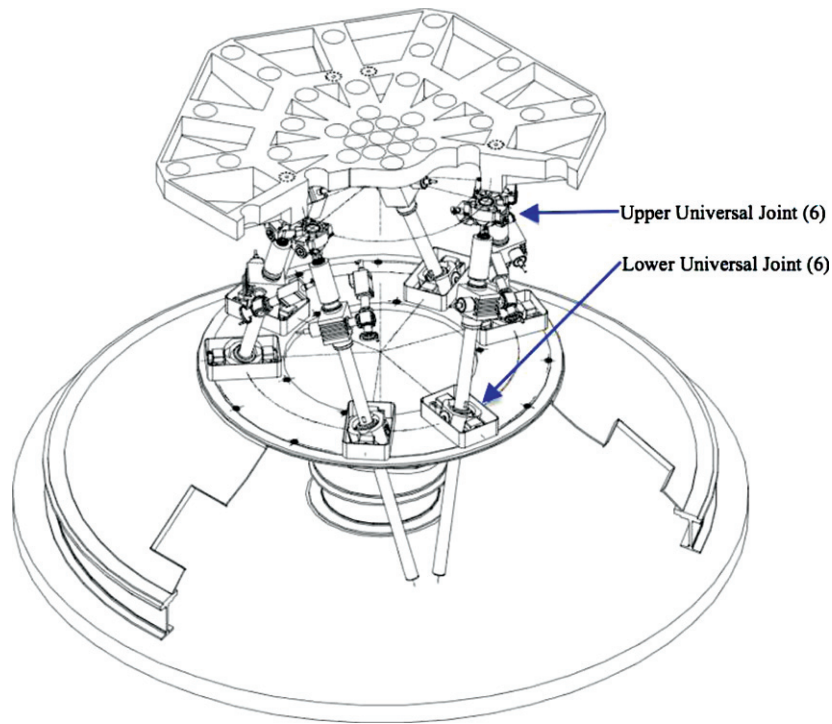


Figure 14. General design of the AMiBA hexapod mount with its main components: support cone, jack screws, u-joints, and platform.

they can also alter the absolute pointing error of each antenna, worsening or improving it due to the local pseudo-random character of the errors. This resultant total pointing error defines the loss in the synthesized beam product (Koch et al. 2008). Due to the complicated position dependence of all these errors, we use a Monte Carlo simulation (10,000 realizations) to quantify the loss. We assume uniformly distributed errors: $p \in [-0.4, 0.4]'$, $d \in [-1, 1]'$, $m \in [-2, 2]'$. The error interval for d is a conservative estimate from the photogrammetry

results, m corresponds to $\sim 10\%$ of the antenna FWHP, which is approximately the achievable mechanical alignment limit. The expected efficiency is about 93%. With $p \in [-1, 1]'$ the efficiency drops to about 90%.

5. CONCLUSION

The hexapod design has some interesting advantages compared to a conventional mount. From an engineering point of

view, it offers a relatively compact design for transportation and possible relocation, a simple cable wrap and ease of access to the receivers from beneath the platform, which is important for daily maintenance and easy reconfiguration of the baselines. For its astronomical application, there is no zenith keyhole, polarization movements are controlled by the same algorithm actuating all six jack lengths and no additional mechanical polarization axis is needed as in the case of the CBI telescope (Padin et al. 2002). Compromises have to be made, leading to a reduced elevation and polarization range of 30° and $\pm 30^\circ$, respectively. Whereas the hexapod offers six degrees of freedom, for its traditional astronomical application only three degrees are used. The AMiBA hexapod is essentially driven along geodesics on a sphere, both for tracking and slewing. Tracking is approximated as a sequence of multiple segments of great circles. Direct and even shorter travel ranges for slewing, following simple translational movements on a straight line, have not been implemented for safety reasons. The hexapod however offers additionally the possibility of small movements along the pointing directions if this should be of astronomical interest.

Pointing with a hexapod is very different from a conventional mount. Position errors are not accumulated as in a serial kinematics system, but the control system is significantly more complex. Utmost care needs to be taken to determine all the jack lengths accurately. With one IT iteration the current pointing accuracy is ~ 0.4 rms in azimuth and elevation, which meets the requirements for the seven-element array compact configuration baselines. An uncompensated pointing error from the platform deformation of the order ~ 0.25 still keeps it in an acceptable range, but needs to be further analyzed for the planned expansion phase. Position errors with polarization movements without IT compensation are typically linearly increasing with polarization as a result of a slight drift of the platform center during the rotation, which is a consequence of the absence of any mechanical polarization axis. This is also compensated with the IT. Laser ranging techniques—along the jack screws or mounted on the ground to determine the orientation of the platform—might be a possible choice to further improve the pointing accuracy of a hexapod.

We thank the anonymous referee for providing useful comments and suggestions. We thank the Ministry of Education, the National Science Council, and the Academia Sinica for their support of this project. We thank the Smithsonian Astrophysical Observatory for hosting the AMiBA project staff at the SMA Hilo Base Facility. We thank the NOAA for locating the AMiBA project on their site on Mauna Loa. We thank the Hawaiian people for allowing astronomers to work on their mountains in order to study the universe. We thank all the members of the AMiBA team for their hard work. Support from the STFC for M.B. and K.L. is also acknowledged.

APPENDIX A

HEXAPOD MAIN COMPONENTS

A.1. Support Cone

The support cone provides stiffness and inertia for the drive system. It consists of three inner and three outer truncated cone steel segments. Individual segments are connected with each other with butt-strap joints for the highest stiffness. Corrosion protection is assured with a three-layer paint system. The anchoring is leveled to about 0.1 . Due to environmental and cost

concerns associated with excavation on Mauna Loa, the cone is not embedded but is sitting on the concrete foundation. A future cone insulation should further improve its thermal behavior. An FEA was done in order to optimize a low structural weight and minimize the pointing error contribution. Simulated load cases included gravity, 10 m s^{-1} side wind, 10 m s^{-1} front wind, a temperature gradient along the cone axis with $\Delta T = 1 \text{ K}$, and a temperature difference between the steel cone and the concrete foundation with $\Delta T = 2 \text{ K}$. In order to separate the pointing error contribution of the support cone from the rest of the telescope, the entire structure above the cone was modeled to be perfectly rigid with no reaction forces. The wind loads were treated as resultant nodal point forces on the platform gravity center. The FEA demonstrated that the contact area between the support cone and concrete foundation is everywhere under pressure in any operational state. The main pointing error contribution then comes from the gravity load with maximum errors at lowest elevation and maximum polarization of about $8''$ and $3''$ in azimuth and elevation, respectively. Temperature gradients (within the cone and between cone and concrete ground) contribute in total about $1''$ to azimuth and elevation pointing errors. 10 m s^{-1} front and side winds can give up to $1''$ pointing error contribution. Generally, the pointing error in both azimuth and elevation increases by about $4''$ to $8''$ if the polarization is changed from 0° to 30° . These errors are calibrated with the help of an IT (Appendix B).

A.2. Universal Joints and Jack Screws

Very stiff and backlash-free u-joints are necessary in order to meet the pointing requirement, because of the high torques under drive conditions, the large shear forces at low elevation, and because u-joint deformation cannot be detected directly. Zero backlash is achieved by tapered roller bearings which are preloaded in the axial direction. A large angular range of motion (partly up to $\pm 52^\circ$) in tangential and radial directions is necessary to achieve the telescope travel range. Minimizing the travel range of the u-joints and jack screws by keeping small dimensions, low weight, and high stiffness has been one of the key design achievements. The end positions of the u-joints are monitored by limit switches which shut off the servo system.

The jack screws consist of a tubular ball screw with an integrated low backlash worm gear with a transmission ratio 10.67:1. Each jack is driven by a motor and a low backlash bevel gear with transmission ratio 4:1. The ball screw spindle of the jack screw is engaged in the worm gear by a backlash-free axial preloaded double nut, which is also free from axial backlash. The jacks, each with a maximum operation load of 100 kN , can be driven at a stroke rate of $0\text{--}20 \text{ mm s}^{-1}$. An absolute (main) angular encoder¹⁶ is mounted at the shaft of the worm gear for an accurate measurement of the jack screw length. If necessary, this can be upgraded with a laser interferometer for a direct measurement of the actual jack screw length, to compensate for errors in the jack screw pitch, the jack elastic deformation and the jack screw and worm gear backlash. It is estimated that this would improve the pointing accuracy from $\sim 10''$ to about $\sim 3''$. Since a hexapod design does not allow for hardware switches to limit the travel range of a telescope, a second set of encoders (auxiliary encoders) has been included

¹⁶ The encoder resolution is $13 \text{ bit} \times 4096 \text{ revolutions}$ with a $\pm 1 \text{ bit}$ accuracy, which leads to a $0.23 \text{ } \mu\text{m}$ overall resolution for a jack pitch of 20 mm . According to the manufacturer's specifications, the measurement inaccuracy is $< 0.1 \text{ } \mu\text{m}$, which has a negligible influence on the pointing error.

for independent determination of jack and telescope positions in a separate safety controller, the HPC (Figure 4).

The jack screws have a minimum and maximum length of about 2.8 m and 6.2 m, respectively, with a maximum travel range of 3.4 m. They can be fully retracted to bring the telescope into a stow position (Figure 1, left panel), which allows us to close the shelter and protect the telescope and instruments from inclement weather and windy conditions. Observations are started with extended jacks from a neutral position (Figure 1, right panel).

A.3. CFRP Platform

The AMiBA platform was designed by ASIAA and fabricated by CMA (Composite Mirror Applications, Inc.), Tucson, AZ, USA. In a segmented approach, the central piece and the six outer elements are bolted together. There are 43 antenna docking positions, allowing for multiple configurations for the array, with baselines from 0.6 to 5.6 m. The receivers are sited behind the antennas and fit through apertures in the platform. The free access to receivers and correlator is shown in Figure 2. Cables and helium lines are guided with a central fixed cable wrap at the back of the platform. An OT for optical pointing tests has been attached to one of the free receiver cells near the upper u-joints. Two photogrammetry surveys in 2005 and 2006 (Raffin et al. 2006) have revealed that the platform deformation during operation is within the specifications of the seven-element compact configuration (Section 4.1).

APPENDIX B

POINTING ERROR MODEL

The pointing corrections on jack level consist of four compensations¹⁷: jack screw pitch error, temperature compensation, jack screw rotation error, and support cone correction.

A jack pitch error correction is essential since the real length of a jack is not directly measured. Only the rotation of the worm gear is measured. Each jack has therefore been calibrated with a correlation function for the exact length against jack screw pitch error compared to the encoder readout. The repeatable measurements are fitted with a polynomial of order 10, leading to a pitch error length correction $\Delta L_{p,i}$ for each jack $i = 1, \dots, 6$, coded in the software:

$$\Delta L_{p,i} \sim \sum_{k=1}^{10} a_{ik} (x_i)^k, \quad (\text{B1})$$

where a_{ik} are the fitting coefficients and x_i is the jack length.

The jack screw length variations due to temperature changes are monitored with three temperature sensors along each jack. The resulting change in length $\Delta L_{T,i}$ is calculated as

$$\Delta L_{T,i} = \int_0^{l_i} \alpha f_i(x) dx, \quad (\text{B2})$$

where $\alpha = 12.0 \times 10^{-6} \text{ K}^{-1}$ is the linear thermal expansion coefficient for ordinary steel and l_i is the position-dependent

length of the jack i . $f_i(x)$ is a linear approximation to the temperature distribution along the jack i :

$$f_i(x) = \begin{cases} \frac{\Delta T_{1,i}}{\Delta T_{2,i} - \Delta T_{1,i}} (P_{2,i} - x) + \frac{\Delta T_{1,i} P_{2,i} - \Delta T_{2,i} P_{1,i}}{P_{2,i} - P_{1,i}} & : x \leq P_{1,i}, \\ \frac{\Delta T_{3,i} - \Delta T_{2,i}}{P_{3,i} - P_{2,i}} (P_{3,i} - x) + \frac{\Delta T_{2,i} P_{3,i} - \Delta T_{3,i} P_{2,i}}{P_{3,i} - P_{2,i}} & : P_{1,i} < x \leq P_{2,i}, \\ \frac{\Delta T_{3,i}}{\Delta T_{3,i}} & : x > P_{3,i}, \end{cases}$$

where P are the positions of the temperature sensors along the jacks. The temperature changes ΔT are calculated with respect to a reference temperature at 17°C .

Because of the spindle thread, a jack screw length change can occur which is not detected by the encoder on the worm gear shaft. Using Euler angles to calculate the kinematics of each jack screw, this undetected rotation β_i can be expressed with respect to a reference angle $\beta_{\text{ref},i}$, yielding a rotation error compensation $\Delta L_{r,i}$ of the form

$$\Delta L_{r,i} = (\beta_{\text{ref},i} - \beta_i) \frac{p}{2\pi}, \quad (\text{B3})$$

where $p = 20 \text{ mm rotation}^{-1}$ is the jack screw pitch.

A support cone compensation model takes into account the deformation of the cone due to temperature changes. The slight shift of the lower fixed u-joints is then calculated by assuming that they expand on concentric circles with a temperature averaged over several sensors in the cone:

$$x_{\text{new}} = x + x \alpha (T - T_0), \quad (\text{B4})$$

$$y_{\text{new}} = y + y \alpha (T - T_0), \quad (\text{B5})$$

where x and y are measured reference coordinates of the lower u-joints at a reference temperature $T_0 = 17^\circ\text{C}$. $\alpha = 12.0 \times 10^{-6} \text{ K}^{-1}$ as for the jack screws. When calculating the required jack lengths from the requested telescope position, this coordinate change results in a slight change of the required jack lengths.

Besides the group of jack screw corrections, a second group of telescope corrections is implemented: radio and optical refraction (e.g., Patel 2000), an OT collimation error correction, and an IT for residual errors. The radio refraction algorithm for the elevation correction $\Delta E_{\text{ref},\text{radio}}$ in radians is taken from Allen (1973):

$$\Delta E_{\text{ref},\text{radio}} = \text{ref}_0 / \tan(El), \quad (\text{B6})$$

where $\text{ref}_0 = (N^2 - 1)/2N^2$ with $N = 1 - (7.8 \times 10^{-5} \times P + 0.39 \times w_v/T)/T$. T , P , and w_v are the temperature in K, the atmospheric pressure in mbar, and the water vapor pressure in mbar, respectively. The calculation of the water vapor pressure w_v is based on the measured relative humidity H on the site:

$$w_v = \frac{H}{100} P_{\text{sat}}$$

where the saturation pressure of the water vapor in mbar is $P_{\text{sat}} = c_0 \times 10^{c_1 \times T/(c_2 + T)}$ with the numerical constants $c_0 = 6.1078$, $c_1 = 7.5$, $c_2 = 237.3$, and the temperature in $^\circ\text{C}$. The optical refraction correction in radians used for optical pointing observations is adopted from Seidelmann (1992) and implemented as

$$\Delta E_{\text{ref},\text{opt}} = 1.2 \times \frac{P}{1013.2} \frac{283.15}{T} \times \frac{60.101 \tan(d_Z) - 0.0668 \tan^3(d_Z)}{(180/\pi)3600}, \quad (\text{B7})$$

¹⁷ Load cells were considered to measure the elastic jack screw deformation due to gravity. Estimates including an FEA predict a maximum length error due to the bending of about $160 \mu\text{m}$ only. The elastic deformation error is therefore not explicitly modeled as a pointing error component, but simply absorbed in the error IT.

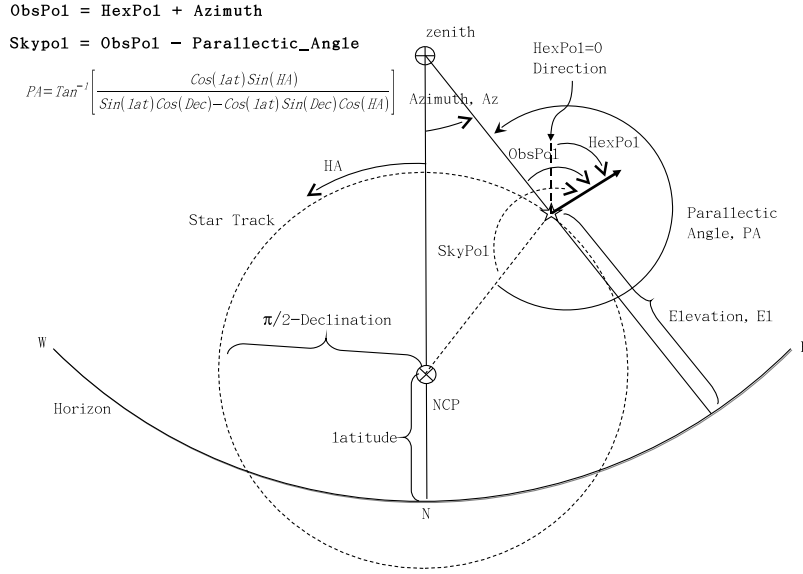


Figure 15. Fundamental angles in astronomy and their relations in the mount and the celestial coordinate systems.

where d_z , P , and T are the distance from the zenith in radians, the atmospheric pressure in mbar, and the ambient temperature in K, respectively.

For both refraction correction modes, we use annually averaged values for the weather data. Extreme weather variations cause changes in the refraction corrections of the order of fractions of arcseconds and are therefore negligible for our wavelength and antenna size.

The OT collimation error is corrected in the form

$$\Delta Az_{OT} = \frac{H_x \cos(\phi_{az} + \phi_{pol}) + H_y \sin(\phi_{az} + \phi_{pol})}{\cos(\phi_{el})}, \quad (B8)$$

$$\Delta El_{OT} = H_y \cos(\phi_{az} + \phi_{pol}) - H_x \sin(\phi_{az} + \phi_{pol}), \quad (B9)$$

where H_x and H_y are the two tilt angles of the OT with respect to the mount pointing axes in the reference plane of the platform. ϕ_{az} and ϕ_{pol} are the mount azimuth and the platform polarization, respectively.

A final pointing correction is done with an IT. Small measured pointing errors which are not explicitly modeled can be entered here. The three-dimensional table yields corrections ΔAz_{IT} , ΔEl_{IT} as a function of Az , El , and $hexpol$ through a linear interpolation. Typically, we build the table with about 100 entries, the largest discontinuities of $\sim 50^\circ$ are at the highest elevations around 85° . Lower elevation with larger errors are resolved at $\sim 20^\circ$.

For the control system, the sums of jack and telescope corrections are then used:

$$\Delta L_{tot,i} = \Delta L_{p,i} + \Delta L_{T,i} + \Delta L_{r,i}, \quad (B10)$$

$$\Delta Az_{tot} = \Delta Az_{IT} + \Delta Az_{OT}, \quad (B11)$$

$$\Delta El_{tot} = \Delta El_{IT} + \Delta El_{OT} + \Delta El_{ref}, \quad (B12)$$

where ΔAz_{tot} and ΔEl_{tot} again lead to an effective change in jack length which is subject to pointing corrections. ΔEl_{ref} is either the radio or optical refraction correction.

All the pointing corrections are calculated on the PTC. From here they are transferred to the ACU in the form described in

Equations (B10)–(B12), illustrated in the flow chart in Figure 3. The ACU applies corrections as

$$L_{act,i} = L_{enc,i} + \Delta L_{tot,i}, \quad (B13)$$

where $L_{enc,i}$ and $L_{act,i}$ are the encoder measured and the real actual length of jack i , respectively. Equally, the actual position (Az_{act} , El_{act}), defined as the real position after applying all the pointing corrections, is displayed on ACU and reported to the remote TCS as

$$Az_{act} = \tilde{Az} + \Delta Az_{tot}, \quad (B14)$$

$$El_{act} = \tilde{El} + \Delta El_{tot}, \quad (B15)$$

where (\tilde{Az}, \tilde{El}) is the telescope position as calculated from the corrected jack lengths $L_{act,i}$ in Equation (B13). The block diagram for the local control system is shown in Figure 4.

APPENDIX C

HEXPOL, SKYPOL, AND THE SKY COORDINATES

The interferometer baselines are fixed with respect to the platform. To describe the platform orientation, we use the mount coordinate system (Az , El , $ObsPol$), where $ObsPol$ refers to the angle between a specified axis on the platform and the line joining the zenith and the current pointing. This specified axis points toward south when the hexapod is in neutral position. The platform rotation is nominally related to the pointing by the relation $ObsPol = Az$. However, the hexapod is capable of changing the rotation by $\pm 30^\circ$ away from this relation. We define the added rotation as $hexpol$ and rewrite the relation as $ObsPol = Az + hexpol$.

The platform orientation can also be written in the sky coordinates (ha , dec , $skypol$), where ha and ra are the hour angle and declination, respectively, in the equatorial coordinate system. $skypol$ thus describes the angle between the specified axis and the line joining the current pointing and the north celestial pole (NCP). The transformation between the two system depends on the latitude (lat) of the observatory as written below. Figure 15 illustrates the relation between the different

angles and the two coordinate systems. The basic transformation relations, including parallactic angle (PA), are

$$\sin(El) = \sin(lat) \sin(dec) + \cos(lat) \cos(dec) \cos(ha),$$

$$\cos(El) \cos(Az) = \cos(lat) \sin(dec) - \sin(lat) \cos(dec) \cos(ha),$$

$$\cos(El) \sin(Az) = -\cos(dec) \sin(ha),$$

$$skypol = obspol - PA,$$

$$PA = \tan^{-1} \left(\frac{\cos(lat) \sin(ha)}{\sin(lat) \cos(dec) - \cos(lat) \sin(dec) \cos(ha)} \right).$$

REFERENCES

- Allen, C. W. 1973, in *Astrophysical Quantities*, ed. A. N. Cox (3rd ed.; Atlantic Highlands, NJ: Humanities Press, Inc.)
- Birkinshaw, M. 1999, *Phys. Rep.*, **310**, 97
- Chen, M.-T., et al. 2009, *ApJ*, 694, 1664
- Chini, R. 2000, *Rev. Mod. Astron.*, **13**, 257
- Gough, V. E. 1956, *Proc. Auto Div. Inst. Mech. Eng.*, 392
- Ho, P. T. P., et al. 2009, *ApJ*, 694, 1610
- Huang, Y.-D., et al. 2008, in *Proc. SPIE 7012, Ground-based and Airborne Telescopes*, ed. L. M. Stepp & R. Gilmozzi (Bellingham, WA: SPIE), 70122H
- Koch, P., et al. 2006, *Proc. EuCAP*, ed. H. Lacoste & L. Ouwehand (ESA SP-626), 668.1
- Koch, P., et al. 2008, in *Proc. SPIE 7018, Advanced Optical and Mechanical Technologies in Telescopes and Instrumentation*, ed. A.-E. Eli, & L. Dietrich (Bellingham, WA: SPIE), 70181L
- Li, C.-T., et al. 2006, in *Proc. SPIE 6275, Submillimeter Detectors and Instrumentation for Astronomy III*, ed. J. Zmuidzinas, W. S. Holland, S. Withington, & W. D. Duncan (Bellingham, WA: SPIE), 627511
- Lin, K.-Y., et al. 2009, *ApJ*, 694, 1629
- Nishioka, H., et al. 2009, *ApJ*, 694, 1637
- Padin, S., et al. 2002, *PASP*, **114**, 83
- Patel, N. A. 2000, in *SMA Technical Memo 139*, <http://sma-www.cfa.harvard.edu/memos/>
- Peacock, J. A. 1999, *Cosmological Physics* (Cambridge: Cambridge Univ. Press)
- Raffin, P., et al. 2006, in *Proc. SPIE 6273, Optomechanical Technologies for Astronomy*, ed. A.-E. Eli, A. Joseph, & L. Dietrich (Bellingham, WA: SPIE), 627311
- Renka, R. J. 1999, *ACM Trans. Math. Softw.*, **25**, 1
- Seidelmann, P. K. 1992, *Explanatory Supplement of the Astronomical Almanac* (Mill Valley, CA: University Science Books)
- Stewart, D. 1965, *UK Inst. Mech. Eng. Proc.*, 180 Pt, 1, 15
- Sunyaev, R. A., & Zel'dovich, Ya. B. 1972, *Commun. Astrophys. Space Phys.*, **4**, 173
- Umetsu, K., et al. 2009, *ApJ*, 694, 1643
- Wu, J. H. P., et al. 2009, *ApJ*, 694, 1619